

Comparison of Dryland Climate Change in Observations and CMIP5 Simulations

JI Mingxia, HUANG Jianping*, XIE Yongkun, and LIU Jun

*Key Laboratory for Semi-Arid Climate Change of the Ministry of Education, College of Atmospheric Sciences,
Lanzhou University, Lanzhou 730000*

(Received 8 December 2014; revised 30 April 2015; accepted 6 May 2015)

ABSTRACT

A comparison of observations with 20 climate model simulations from the Coupled Model Intercomparison Project, Phase 5 (CMIP5) revealed that observed dryland expansion amounted to $2.61 \times 10^6 \text{ km}^2$ during the 58 years from 1948 to 2005, which was four times higher than that in the simulations ($0.55 \times 10^6 \text{ km}^2$). Dryland expansion was accompanied by a decline in aridity index (AI) (drying trend) as a result of decreased precipitation and increased potential evapotranspiration across all dryland subtype areas in the observations, especially in the semi-arid and dry subhumid regions. However, the CMIP5 multi-model ensemble (MME) average performed poorly with regard to the decreasing trends of AI and precipitation. By analyzing the factors controlling AI, we found that the overall bias of AI in the simulations, compared with observations, was largely due to limitations in the simulation of precipitation. The simulated precipitation over global drylands was substantially overestimated compared with observations across all subtype areas, and the spatial distribution of precipitation in the MME was largely inconsistent in the African Sahel, East Asia, and eastern Australia, where the semi-arid and dry subhumid regions were mainly located.

Key words: aridity index, dryland expansion, climate change, CMIP5

Citation: Ji, M. X., J. P. Huang, Y. K. Xie, and J. Liu, 2015: Comparison of dryland climate change in observations and CMIP5 simulations. *Adv. Atmos. Sci.*, **32**(11), 1565–1574, doi: 10.1007/s00376-015-4267-8.

1. Introduction

Drylands, which are characterized by scarce and highly variable precipitation that does not compensate for the evaporative demands (Reynolds et al., 2007), cover approximately 41% of Earth's land surface and are inhabited by more than one third of the world's population (35.5% of the global population in the year 2000) (Safriel et al., 2005). The dry climate of drylands (Huang et al., 2008, 2010; Wang et al., 2008, 2010, 2015; Nicholson, 2011; Maestre et al., 2012), coupled with the relatively low fertility of their soils (Reynolds et al., 2007; Li et al., 2009), forms fragile ecosystems that are sensitive to climate change and human activities (Charney, 1975; Georgescu et al., 2009). Increases in temperature and changes in precipitation patterns are two important components of climate change that are of particular interest for drylands (Bader and Latif, 2003; Giannini et al., 2003; Giannini, 2010; Huang et al., 2012; Wallace et al., 2012; He et al., 2014; Ji et al., 2014).

There is general agreement among most models that warming of over 3°C is expected for drylands by the end of the 21st century [Intergovernmental Panel on Climate Change (IPCC), 2013]. Zhao et al. (2014) reported that ongoing

warming projected by the Coupled Model Intercomparison Project, Phase 5 (CMIP5) multi-model ensemble (MME) over arid and semi-arid areas can clearly be seen under different representative concentration pathways (RCPs). However, projections of changes in precipitation are subject to a greater degree of uncertainty than are those of temperature. Kumar et al. (2014) suggested that the agreements among the CMIP5 models are higher in simulation of the mean pattern and amplitude for temperature than in that of precipitation. A multi-model analysis projected variations in annual precipitation of -30% to 25% in drylands, depending on the dryland region considered (Bates et al., 2008). Zhao et al. (2014) reported that precipitation is expected to increase by more than 40% under RCP4.5 over central Asia and the Sahara/Sahel, but precipitation will be reduced over the Mediterranean. Potential evapotranspiration (PET), representing the evaporative demand of the atmosphere, is also projected to increase (IPCC, 2013). This is because the water-holding capacity of the atmosphere increases with higher temperatures, but precipitation and relative humidity are not projected to change significantly on the global scale (IPCC, 2013). As a result, the water vapor deficit in the atmosphere will increase, and PET will increase (Trenberth et al., 2003). As a consequence of such expected climatic changes, drying is expected to occur in a substantial portion of drylands. Moreover, droughts may become longer lasting and more severe (Dai, 2011, 2013),

* Corresponding author: HUANG Jianping
Email: hjp@lzu.edu.cn

and the drylands will become drier in warmer climates, such as western North America (Seager et al., 2007; Hughes and Diaz, 2008), the Mediterranean Basin (Giorgi and Lionello, 2008; Mariotti et al., 2008), southern Africa (Haensler et al., 2011), and Australia (Hughes, 2011).

It has been considered that such drying patterns in drylands result from global warming, which leads to intensification of the hydrological cycle, with climatologically wet regions becoming wetter and dry regions becoming drier (Neelin et al., 2003; Trenberth et al., 2003; Held and Soden, 2006; Chou et al., 2009; Seager et al., 2010). Therefore, in a standard IPCC-style simulation, the area of the world's desert areas is predicted to increase by $\sim 10\%$ by the end of the 21st century (Zeng and Yoon, 2009). This projection is supported by a recent study by Feng and Fu (2013), which also projected that global drylands will expand by $\sim 10\%$ by 2100 based on simulations from CMIP5. As mentioned above, there are many future projection results for drylands. However, it is noteworthy that the extent of dryland expansion is underestimated in the CMIP5 historical simulations. Although the evidence from both observations and the historical simulations of CMIP5 models indicates that drylands expanded during the 58 years from 1948 to 2005, the expansion in drylands shown by the simulations is only one-fourth of that observed. Therefore, before the model projections can be trusted, it is critical to evaluate the ability of these models to simulate 20th century variability in dryland expansion and climate change, which is the foundation of their ability to project the future. In the present study, we focused on analyzing the observed area and climate changes in drylands and compared them with model-simulated changes to improve our understanding of dryland climate change.

2. Data and methods

2.1. Classification of drylands

Different criteria and climate classification schemes have been used to define the climatic boundaries of drylands and their subtypes (Thornthwaite, 1948; Meigs, 1953; Ma and Fu, 2003; Kottek et al., 2006; Huang et al., 2012; Feng and Fu, 2013). The fundamental commonality in most climatic definitions of drylands is the balance between precipitation and PET. Following Middleton and Thomas (1997), in this study, drylands were defined as regions with aridity index (AI), which is the ratio of annual precipitation to annual PET, of <0.65 . Drylands were classified into four subtypes of hyper-arid ($AI < 0.05$), arid ($0.05 < AI < 0.2$), semi-arid ($0.2 < AI < 0.5$), and dry subhumid ($0.5 < AI < 0.65$).

2.2. Observation-based PET

There are very limited direct measurements of PET available (Abtew et al., 2011); thus, PET must be inferred for climate studies. Two methods are widely used to estimate PET. One is the Thornthwaite method (Thornthwaite, 1948; Middleton and Thomas, 1997), which is an empirical formula that defines PET as a function of the mean monthly temperature.

However, temperature is not always the primary factor controlling PET (Donohue et al., 2010; Shaw and Riha, 2011; Hobbins et al., 2012), which is also influenced by radiative and aerodynamic controls (Penman, 1948). The other approach to defining PET is the Penman–Monteith algorithm, which considers many climate factors related to the evapotranspiration process, such as solar radiation, relative humidity, temperature, and wind (Allen et al., 1998). This algorithm is derived from physical principles and is superior to empirically based formulations that usually only consider the effect of temperature (Feng and Fu, 2013).

The PET data used in this study were provided by Feng and Fu (2013) and were calculated using the Penman–Monteith method (Allen et al., 1998). To calculate PET, the solar radiation, specific humidity, and wind speed reanalysis datasets from the Global Land Data Assimilation System (GLDAS), as well as the observed monthly surface air temperature (SAT) dataset, were used. The GLDAS datasets have global coverage with $0.5^\circ \times 0.5^\circ$ latitude–longitude resolution starting from 1948 (Rodell et al., 2004). The observed SAT dataset was developed by the National Centers for Environmental Prediction (NCEP)/Climate Prediction Center (CPC) (Fan and Van den Dool, 2008). It comprises station-based observation data covering global land areas with a spatial resolution of $0.5^\circ \times 0.5^\circ$ for the period from 1948 to 2005, and it is referred to as the GHCN_CAMS gridded 2 m temperature dataset. In this study, PET calculated with observed and reanalysis datasets is referred to as observation-based PET.

2.3. Observed precipitation datasets

In addition to the SAT dataset, we used the corresponding precipitation dataset from the NCEP/CPC, which is referred to as the Precipitation Reconstruction over Land (PREC/L; Chen et al., 2002). This dataset has the same temporal coverage and spatial resolution as the GHCN_CAMS gridded 2 m temperature dataset. To better illustrate the reliability of using the PREC/L dataset, trends in land precipitation have been analyzed using a number of datasets; notably, the Climate Research Unit (CRU) at the University of East Anglia (Mitchell and Jones, 2005), the Global Precipitation Climatology Centre (GPCC) full data reanalysis, version 6 (Schneider et al., 2013; Zhao et al., 2014), and the University of Delaware dataset (UDel; Legates and Willmott, 1990). The GPCC, CRU, and UDel datasets have the same spatial and temporal coverage as PREC/L.

The spatial distributions of the precipitation trends in dryland regions using the four datasets (figure not shown) indicated that the patterns of the linear trends of precipitation were in good agreement, with only small differences among the datasets. Additionally, the dryland averaged temporal variations in precipitation generally decreased in the 56 years from 1948 to 2005, based on the four datasets (figure not shown); the precipitation decline ranged from 0.9 to $3.1 \text{ mm (10 yr)}^{-1}$ depending on the dataset, although none of the trend estimates was significant. The results showed that the linear trends of precipitation were in good agreement in the spatial distributions and regionally averaged temporal vari-

ations over drylands. However, it should be noted that the observed precipitation data in hyper-arid regions may not be very reliable due to poor data coverage (Chen et al., 2002), such as the Sahara Desert, the Arabian Peninsula, and the Taklimakan Desert.

2.4. Model simulations

The historical simulations from CMIP5 are forced with natural solar and volcanic variations and anthropogenic radiative forcings; most of these simulations cover the period from 1850 to 2005 (Taylor et al., 2012). Here, the historical simulations of 20 CMIP5 climate models (Table 1) were selected (Taylor et al., 2012), and we only analyzed the period starting from 1948, when both observed and reanalysis datasets were available. The ensemble mean of the 20 models was analyzed because the MME average is considered superior to individual models (Pierce et al., 2009; Zhao et al., 2014). The first ensemble run was used if a model has multiple ensemble simulations. All of the simulated temperature, precipitation, solar radiation, specific humidity, and wind speed values were statistically downscaled to half-degree resolution, as in Feng and Fu (2013).

Table 1. The 20 CMIP5 models used in this study.

Model name	Modeling center
BCC-CSM1.1	Beijing Climate Center, China
CanESM2	Canadian Centre for Climate, Canada
CCSM4	National Center for Atmospheric Research, USA
CNRM-CM5	Le Centre National de Recherches Météorologiques, France
CSIRO-Mk3.6.0	Commonwealth Scientific and Industrial Research, Australia
GFDL-CM3	Geophysical Fluid Dynamics Laboratory, USA
GFDL-ESM2G	Geophysical Fluid Dynamics Laboratory, USA
GFDL-ESM2M	Geophysical Fluid Dynamics Laboratory, USA
GISS-E2-R	NASA Goddard Institute for Space Studies, USA
HadGEM2-CC	Met Office Hadley Centre, UK
HadGEM2-ES	Met Office Hadley Centre, UK
INM-CM4	Institute for Numerical Mathematics, Russia
IPSL-CM5A-LR	L'Institut Pierre-Simon Laplace, France
IPSL-CM5A-MR	L'Institut Pierre-Simon Laplace, France
MIROC-ESM	Japan Agency for Marine-Earth Science and Technology, Japan
MIROC-ESM-CHEM	Japan Agency for Marine-Earth Science and Technology, Japan
MIROC5	Atmosphere and Ocean Research Institute, Japan
MPI-ESM-LR	Max Planck Institute for Meteorology, Germany
MRI-CGCM3	Meteorological Research Institute, Japan
NorESM1-M	Norwegian Climate Centre, Norway

3. Results

Figure 1 shows the spatial distribution of drylands and its subtypes for the 1961–90 climatology defined by AI, which is consistent with the results from Feng and Fu (2013). As shown in Fig. 1, major hyper-arid areas generally occurred over the deserts, such as the Sahara Desert, the Rub al Khali Desert in the eastern Arabian Peninsula, and the Taklimakan Desert. Arid areas were mainly located over Central Asia and much of Australia. Semi-arid and dry subhumid regions were located outside the hyper-arid and arid regions, such as in the western United States, Central and East Asia, and a large portion of Australia. As indicated by Safriel et al. (2005), drylands accounted for 41% of the global land surface.

Recent observations and model simulations indicate that global drylands have expanded remarkably, and the expansion will continue in the 21st century (Feng and Fu, 2013). Despite large differences between observations and model simulations, Feng and Fu (2013) reported that the models were able to simulate the robust expansion of drylands. To further evaluate the simulation capability of the CMIP5 models compared with observations, we compared the time series of area change for drylands and subtypes in observations and the ensemble mean of the historical simulations of 20 CMIP5 models (Fig. 2). Generally, the global drylands in the observations expanded remarkably during the 58 years from 1948 to 2005, especially since the 1980s (Fig. 2a). However, the simulations of the area change in drylands were not consistent with observations. The area changes for dryland subtype regions in the simulations were also inconsistent with observations (Figs. 2b–e). For instance, the dry subhumid regions have evidently expanded since the mid-1980s, and the semi-arid regions show evident expansion in the late 1960s; however, the CMIP5 MME did not capture these changes. Naturally, we must therefore question what factor it is that leads to the large biases (or differences) between the observations and simulations.

To understand the differences between the observations and CMIP5 MME simulations of area changes in dryland regions and subtypes during the 58-year study period, two subperiods were chosen: the first 15 years (1948–62) and the most recent 15 years (1991–2005). Table 2 shows the

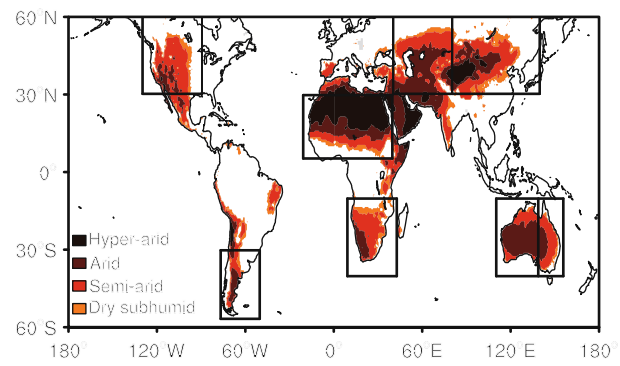


Fig. 1. Global distribution of drylands during 1961–90 according to AI.

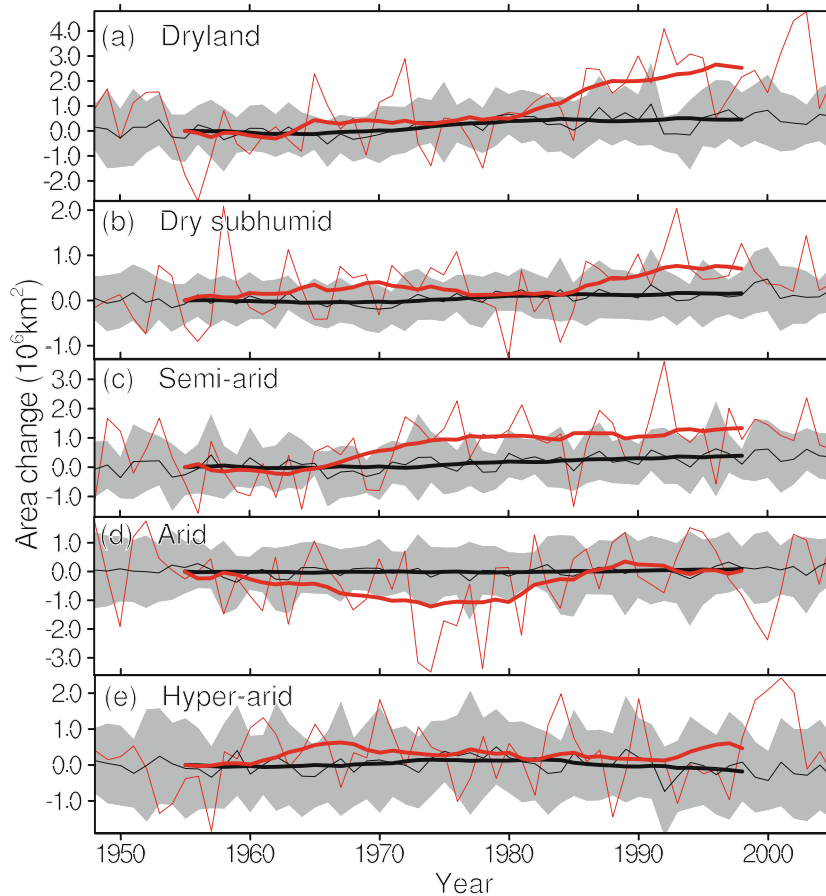


Fig. 2. Temporal variations in area change for (a) total drylands and (b) dry subhumid, (c) semi-arid, (d) arid, and (e) hyper-arid regions, with respect to the mean values from 1948–62. The thin red curve is based on observations. The thin black curve is the CMIP5 MME. The grey shading denotes one standard deviation of the historical simulations. The 15-year running smooth (thick) curves were applied to emphasize climate change.

Table 2. The area change, in units of 10^6 km^2 , by climate type for 1991–2005 compared to 1948–1962 from observations (CMIP5 MME).

Climate type	Net change	To wetter type	To drier type	
Hyper-arid	0.61 (0.0)	Hyper-arid to arid	0.37 (0.0)	N/A
Arid	−0.12 (−0.10)	Arid to semi-arid	1.11 (0.20)	Arid to hyper-arid 0.98 (0.0)
Semi-arid	1.58 (0.15)	Semi-arid to dry subhumid	0.87 (0.38)	Semi-arid to arid 1.60 (0.10)
		Semi-arid to humid	0.01 (0.31)	
dry subhumid	0.50 (0.50)	dry subhumid to humid	0.96 (0.37)	dry subhumid to semi-arid 2.84 (0.22)
Humid	−2.61 (−0.55)	N/A		Humid to dry subhumid 3.47 (0.71)
				Humid to semi-arid 0.11 (0.52)

transitions in the drylands between these two periods. The simulated dryland area for the most recent 15 years (1991–2005) was only $0.55 \times 10^6 \text{ km}^2$ larger than that for the period 1948–62, which was only one-fourth of the observed expansion ($2.61 \times 10^6 \text{ km}^2$), indicating that dryland expansion was severely underestimated in the simulations. For specific dryland subtypes, the areas expanded in most subtype regions, except for arid regions, which decreased both in the observations and the CMIP5 MME. The largest difference occurred

in the semi-arid regions, where the observed area increased by $1.58 \times 10^6 \text{ km}^2$, accounting for more than half of the total dryland expansion, whereas the semi-arid regions expanded by only $0.15 \times 10^6 \text{ km}^2$ according to the CMIP5 MME simulation, just one-tenth of the observed expansion. The hyper-arid region also showed major differences; the observed area of the hyper-arid region expanded by $0.61 \times 10^6 \text{ km}^2$, which was transitioning from arid regions, whereas there was no change according to the CMIP5 MME simulation. The ar-

eas in arid and dry subhumid regions changed (in units of 10^6 km^2) by -0.12 (-0.1) and 0.5 (0.5) in the observations (CMIP5 MME). In these two subtype areas, the simulated area changes were comparable to the observed changes. The total area of land (including drylands and humid regions) that changed to drier subtypes, was $9 \times 10^6 \text{ km}^2$ ($1.56 \times 10^6 \text{ km}^2$) in the observations (CMIP5 MME), whereas the total area of drylands that transitioned to wetter subtypes was $3.32 \times 10^6 \text{ km}^2$ ($1.26 \times 10^6 \text{ km}^2$).

Figure 3 presents the time series of regionally averaged precipitation, PET, AI, and SAT in hyper-arid, arid, semi-arid, and dry subhumid regions during 1948–2005, and Table 3 shows the linear trends. As indicated in Figs. 3a–d, precipitation decreased with large annual variability across all dryland subtypes in the observation, especially over semi-arid and dry subhumid regions, where the change rates were -4.33 and $-6.48 \text{ mm (10 yr)}^{-1}$, respectively, and were significant at the 95% confidence level. However, the CMIP5 MME simulations showed positive trends in precipitation across all dryland subtypes except the dry subhumid regions. Given that AI is defined as the ratio of precipitation to PET, PET is another key component affecting changes in AI. As shown in Figs. 3e–h, the time series of PET in the MME was

consistent with the observations across all dryland subtype regions. PET increased in all dryland subtype regions in both the observations and the MME, and all of the positive trends were significant, except for observations in the hyper-arid region. As shown in Table 3, the trends of SAT were significantly positive over all of the dryland subtype areas in both the observations and the MME; however, the trends in the MME was smaller than in the observations. As expected, the variability of AI declined (drying) as a result of decreased precipitation and increased PET across all dryland areas in the observations, especially in the semi-arid and dry subhumid regions (Figs. 3i–l), where the negative trends were significant at the 99% confidence level. However, the negative trends in the semi-arid and dry subhumid regions were much weaker in the simulations, and a positive trend was identified in the arid region (Table 3). Considering that the observation-based PET was well simulated in these regions, the weaker drying trends in the MME were primarily the result of the simulated precipitation.

Figure 4 demonstrates the patterns of linear trends in precipitation, PET, AI, and SAT over drylands during 1948–2005 in the observations and simulations. The observed precipitation was characterized by significant decreasing trends

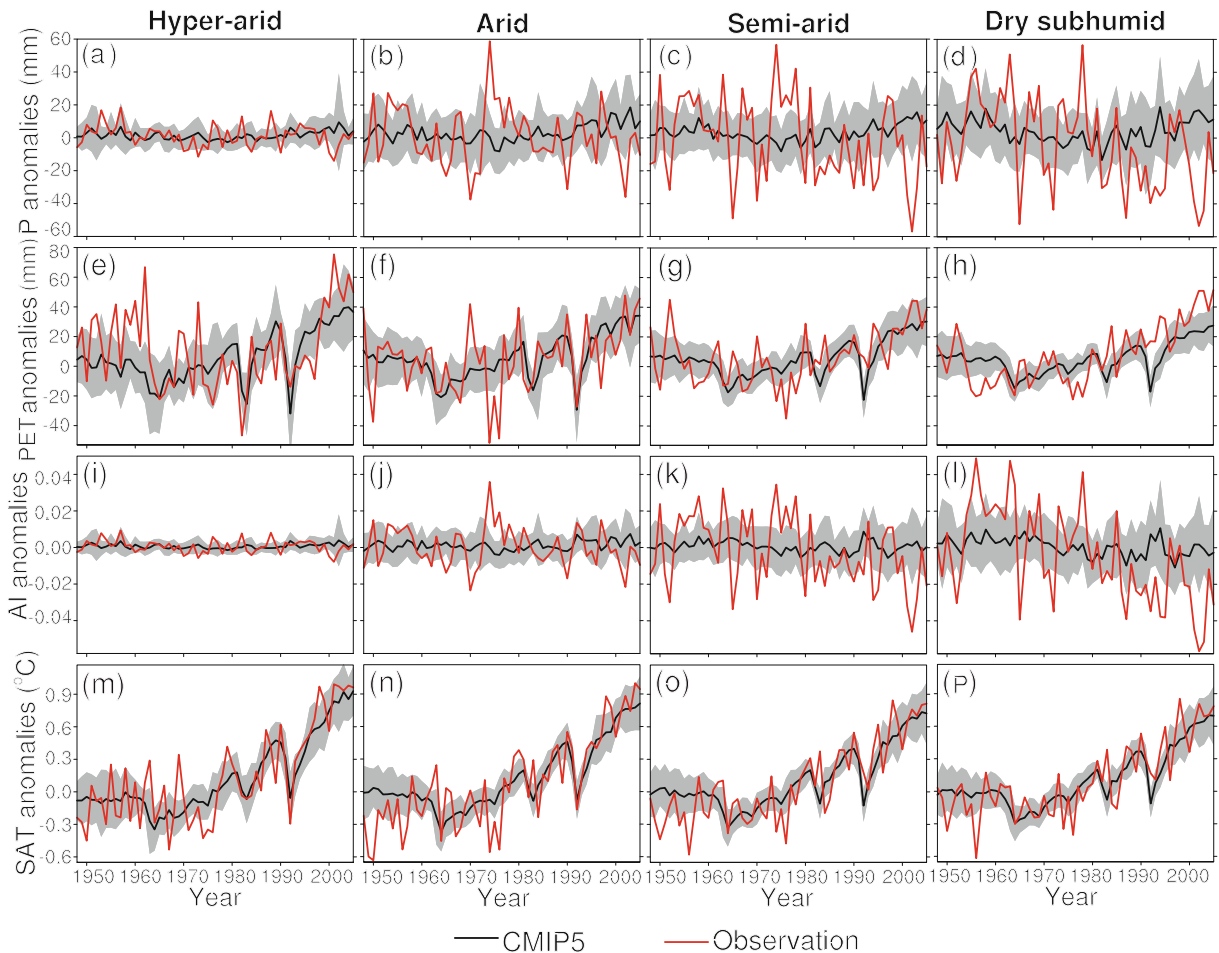


Fig. 3. Temporal variations in regionally averaged precipitation (P), PET, AI, and SAT in hyper-arid, arid, semi-arid, and dry subhumid regions from observations (red) and the CMIP5 MME (black). The mean for 1961–90 was removed from each variable.

Table 3. Trends of regionally averaged precipitation, PET, AI, and SAT in hyper-arid, arid, semi-arid, and dry subhumid regions from observations (CMIP5). One asterisk denotes the trend is significant at the 95% confidence level, and two denotes the trend is significant at the 99% confidence level.

Climate type	Precipitation [mm (10 yr) $^{-1}$]	PET [mm (10 yr) $^{-1}$]	AI (10 yr) $^{-1}$	SAT [$^{\circ}$ C (10 yr) $^{-1}$]
Hyper-arid	−0.72 (0.39)	2.03 (6.00**)	−0.0003 (0.0001)	0.19** (0.17**)
Arid	−1.33 (1.41**)	3.85* (4.55**)	−0.0010 (0.0004*)	0.20** (0.14**)
Semi-arid	−4.33* (0.87*)	4.29** (3.86**)	−0.0041** (−0.0004)	0.17** (0.13**)
Dry subhumid	−6.48** (−0.10)	7.60** (3.10**)	−0.0084** (−0.0015**)	0.15** (0.12**)

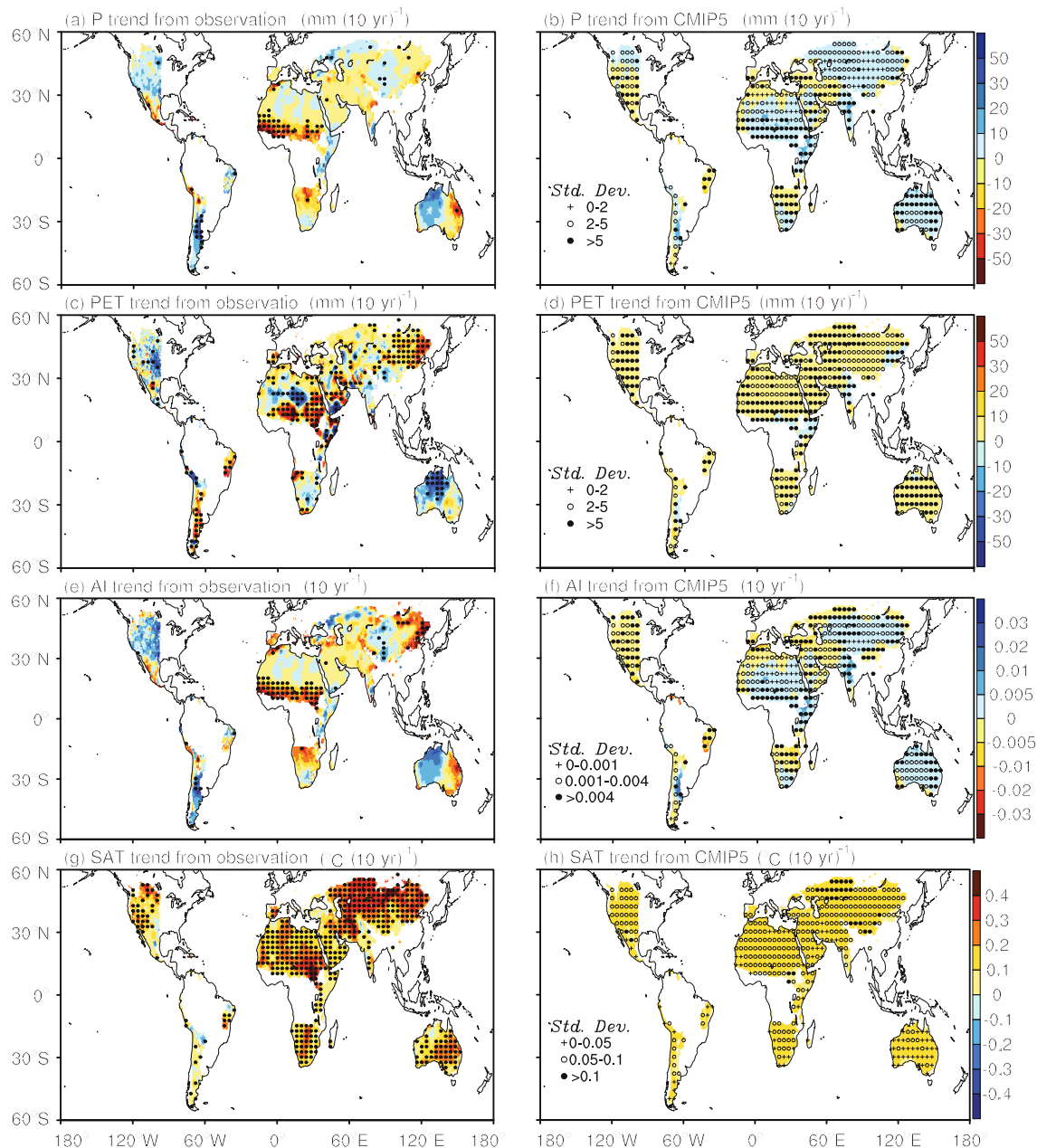


Fig. 4. Linear trends in precipitation (P), PET, AI, and SAT in drylands from 1948 to 2005 in observations (left-hand panels) and the CMIP5 MME (right-hand panels). Stippling in the observations indicates that the observed trend was significant at the 99% confidence level, as determined by a two-sided Student's *t*-test. Crosses, open circles, and filled circles in the CMIP5 MME denote one standard deviation of the 20 CMIP5 models.

in drylands across the African Sahel, southern Africa, Central Asia, some of East Asia, and eastern Australia, and by increasing tends over the central United States, Argentina, and west/central Australia (Fig. 4a). However, most of the observed negative trends were not captured by the CMIP5 MME (Fig. 4b). In fact, the models showed opposite trends (increasing precipitation) over these regions. Although the models did capture the positive trend over western Australia, the trend was smaller than that observed. Comparing Figs. 4a and b, the precipitation pattern in the MME was largely inconsistent in the African Sahel, East Asia, and eastern Australia, where the semi-arid and dry subhumid regions were mainly located. This result is also consistent with previous studies (Zhao et al., 2014). For example, Zhao et al. (2014) indicated that models underestimated the long-term trend in global precipitation and did not capture the observed features of precipitation in certain areas. Although linear trends for regional averaged PET were well simulated in all dryland subtype regions (Figs. 3e–h), the PET patterns showed large differences between observations and the MME (Figs. 4c and d). The observed PET increased evidently over East Asia and the African Sahel and decreased in the central United States, the central Sahara, and western Australia, whereas PET in the MME showed a uniform increase in drylands. The patterns of AI were similar to precipitation patterns in both the observations and the MME, but with some regional differences (Figs. 4a and e). Large inconsistencies in AI between the observations and simulations could be found for the African Sahel, East Asia, Australia, and the American continents. As Figs. 4g–h indicate, significant positive trends in SAT were apparent across most drylands in both the observations and the MME, but SAT was much warmer in the observations than in the simulations, especially in northern Central Asia, East Asia, and the African Sahel (Figs. 4g and h).

To quantify the differences between observations and simulations, the changes in regionally averaged precipitation, PET, and AI in the simulations and observations over global drylands and eight typical dryland regions [East Asia, Central Asia, northern Africa, North America, South America, southern Africa, western Australia, and eastern Australia (labeled in Fig. 1)] during 1948–2005 were calculated; the differences are shown in Fig. 5. For global drylands, the simulated precipitation was overestimated across all subtype regions compared with the observations, especially in the semi-arid and dry subhumid regions, where precipitation was overestimated by as much as 30 and 37 mm (58 yr)⁻¹, respectively (Fig. 5a). AI was overestimated across all subtypes, especially in the semi-arid and dry subhumid regions, where PET was underestimated. In the specific dryland regions, simulated precipitation was overestimated over most of the typical regions (East Asia, Central Asia, northern Africa, southern Africa, and eastern Australia) compared with the observations, whereas simulated precipitation was underestimated over the other three typical dryland regions, especially South America. The simulated PET was evidently underestimated over East Asia, South America, and most regions in north-

ern Africa, except hyper-arid regions, whereas the simulated PET was overestimated over North America and eastern Australia. As a result, AI was overestimated in most of the typical regions (East Asia, Central Asia, southern Africa, northern Africa, and eastern Australia), where precipitation was overestimated, and AI was underestimated in the other three regions, where precipitation was underestimated. It is interesting that the over- or underestimation of AI in specific regions was consistent with the over- or underestimation of precipitation, regardless of whether the PET was over- or underestimated, indicating that discrepancies in precipitation played a dominant role in the large discrepancies in AI between the observations and MME in all the typical regions. Therefore, we conclude that it may be possible to reduce the differences between observed and simulated AI in drylands if future improvements can be made to the models' simulation of regional precipitation.

4. Conclusion and discussion

In this study, we investigated the historical area changes and climate changes of drylands and subtype regions using both observational datasets and CMIP5 simulations for the period 1948–2005. Generally, the global drylands in the observations expanded remarkably during the 58 years; however, this expansion was severely underestimated in the CMIP5 MME. The dryland expansion was accompanied by a drying trend (AI decreasing) as a result of decreased precipitation and increased potential evapotranspiration (PET). Although the increasing trends of observation-based PET were simulated well in global drylands, the CMIP5 MME did not perform well in capturing the observed decreasing trends of AI and precipitation across all dryland subtype areas. The precipitation pattern in the MME was largely inconsistent in the African Sahel, East Asia, and eastern Australia, where the semi-arid and dry subhumid regions were mainly located. On the global scale, the simulated precipitation was overestimated compared with observations across all subtype areas, especially in the semi-arid and dry subhumid regions. In specific dryland regions, AI was overestimated or underestimated consistently, with over- or underestimation of precipitation, regardless of whether PET was over- or underestimated. Thus, we conclude that the overall bias of AI in the simulations, compared with observations, was largely due to limitations in the simulation of precipitation on the regional scale. One potential reason for the underestimation of precipitation could be that the trend in precipitation in the simulations was smoothed by the MME. Plus, it may partly have been caused by variation in individual models' simulation capabilities and deficiencies. Recent studies also demonstrate that the large uncertainties in precipitation are mainly caused by natural variations in sea surface temperatures, which are often not captured by climate models (Dai, 2013). The uncertainty in simulated precipitation over these regions may be driven by other mechanisms such as the different convection and microphysical parameterization schemes (Huang et al.,

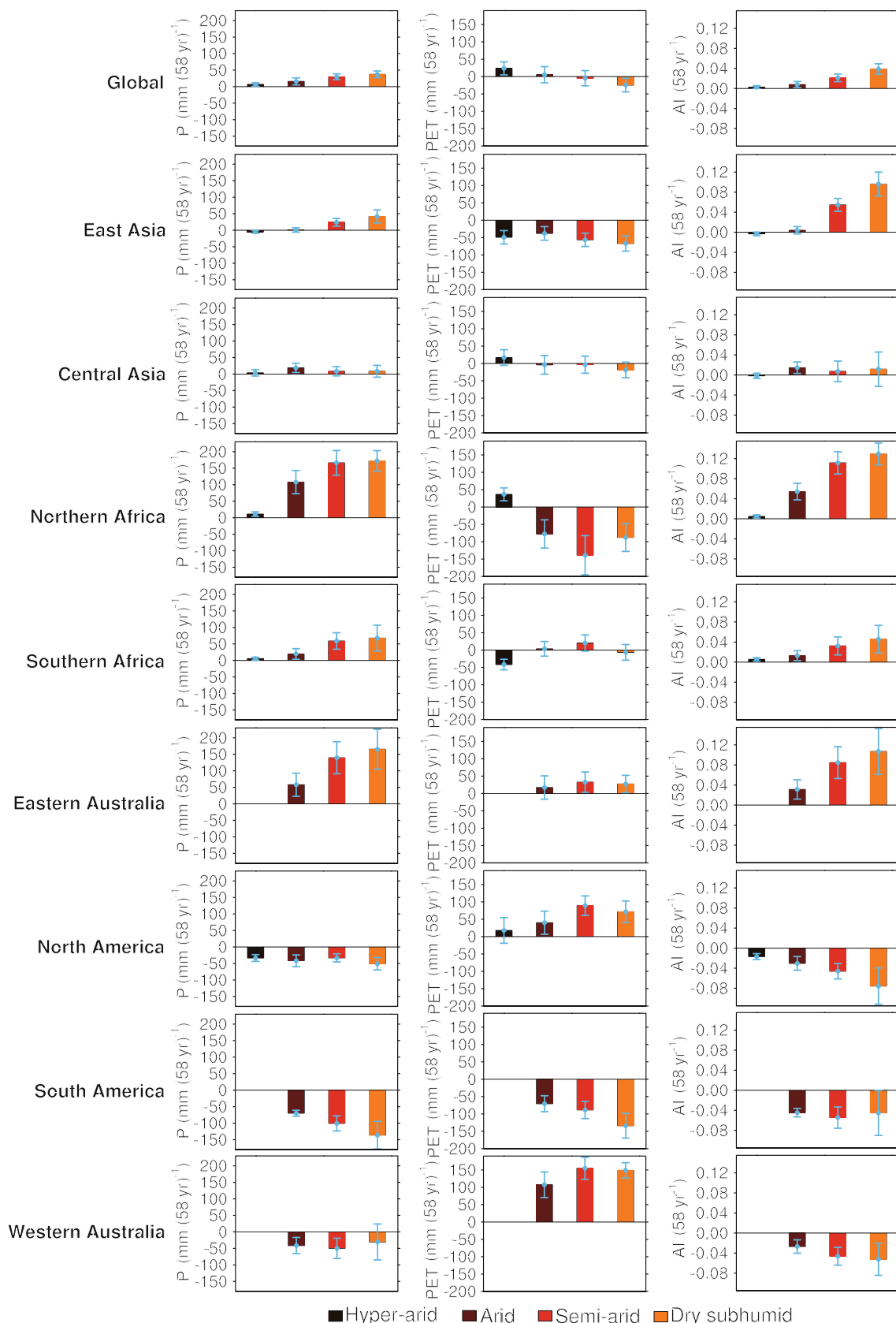


Fig. 5. Differences between observations and the CMIP5 MME for changes in regionally averaged precipitation (P), PET, and AI in hyper-arid, arid, semi-arid, and dry subhumid regions during 1948–2005 in global drylands and East Asia, Central Asia, northern Africa, southern Africa, eastern Australia, North America, South America, and western Australia. The error bars indicates one standard deviation of the 20 CMIP5 models.

2013), or by the uncertainty in decadal to multidecadal variability (Ault et al., 2012), and result from biases in data assimilations and model resolutions (Kimoto, 2005; Kusunoki et al., 2006). As the CMIP5 MME cannot capture the observed variability of dryland precipitation, further investigations are needed to validate the regional precipitation simulation capability of specific models.

Acknowledgements. This work was jointly supported by the National Basic Research Program of China (Grant No. 2012CB955301), the National Science Foundation of China (Grant Nos. 41175134 and 41305060), and the Program for Changjiang Scholars and Innovative Research Team in University (Grant No. IRT1018). We thank Prof. S. FENG and Prof. Q. FU for providing the PET datasets. We also acknowledge the CMIP5 climate modelling groups, for producing and making their model output available. The original CMIP5 data were provided by the Earth System Grid Federation (ESGF) and are available at <http://pcmdi9.llnl.gov/esgf-web-fe/live#>. The CPC data are available from the Physical Sciences Division of NOAA's Earth System Research Laboratory: <http://www.esrl.noaa.gov/psd/data/gridded/>. The CRU data are available from the CRU's data center at the University of East Anglia: <http://www.cru.uea.ac.uk/cru/data/hrg/tmc/>.

REFERENCES

Abtew, W., J. Obeysekera, and N. Ircanin, 2011: Pan evaporation and potential evapotranspiration trends in South Florida. *Hydrological Processes*, **25**, 958–969.

Allen, R. G., L. S. Pereira, D. Raes, and M. Smith, 1998: Crop evapotranspiration: Guidelines for computing crop water requirements, FAO Irrigation and Drainage Paper, No. 56.

Ault, T. R., J. E. Cole, and S. St. George, 2012: The amplitude of decadal to multidecadal variability in precipitation simulated by state-of-the-art climate models. *Geophys. Res. Lett.*, **39**, L21705, doi: 10.1029/2012GL053424.

Bader, J., and M. Latif, 2003: The impact of decadal-scale Indian Ocean sea surface temperature anomalies on Sahelian rainfall and the North Atlantic Oscillation. *Geophys. Res. Lett.*, **30**, 2169–2172, doi: 10.1029/2003GL018426.

Bates, B. C., Z. W. Kundzewicz, S. Wu, and J. P. Palutikof, 2008: *Climate Change and Water*. Intergovernmental Panel on Climate Change Secretariat, Geneva, 210 pp.

Charney, J. G., 1975: Dynamics of deserts and drought in the Sahel. *Quart. J. Roy. Meteor. Soc.*, **101**, 193–202.

Chen, M., P. Xie, J. E. Janowiak, and P. A. Arkin, 2002: Global land precipitation: A 50-yr monthly analysis based on gauge observations. *J. Hydrometeorol.*, **3**, 249–266.

Chou, C., J. David Neelin, C.-A. Chen, and J.-Y. Tu, 2009: Evaluating the “rich-get-richer” mechanism in tropical precipitation change under global warming. *J. Climate*, **22**, 1982–2005.

Dai, A. G., 2011: Drought under global warming: A review. *Wiley Interdisciplinary Reviews: Climate Change*, **2**, 45–65.

Dai, A. G., 2013: Increasing drought under global warming in observations and models. *Nature Climate Change*, **3**, 52–58.

Donohue, R. J., T. R. McVicar, and M. L. Roderick, 2010: Assessing the ability of potential evaporation formulations to capture the dynamics in evaporative demand within a changing climate. *J. Hydrol.*, **386**, 186–197.

Fan, Y., and H. Van den Dool, 2008: A global monthly land surface air temperature analysis for 1948–present. *J. Geophys. Res. (Atmos.)*, **113**, D01103, doi: 10.1029/2007JD008470.

Feng, S., and Q. Fu, 2013: Expansion of global drylands under a warming climate. *Atmospheric Chemistry and Physics*, **13**, 10081–10094.

Georgescu, M., G. Miguez-Macho, L. T. Steyaert, and C. P. Weaver, 2009: Climatic effects of 30 years of landscape change over the Greater Phoenix, Arizona, region: 1. Surface energy budget changes. *J. Geophys. Res. (Atmos.)*, **114**, D05110, doi: 10.1029/2008JD010745.

Giannini, A., 2010: Mechanisms of climate change in the semiarid African Sahel: The local view. *J. Climate*, **23**, 743–756.

Giannini, A., R. Saravanan, and P. Chang, 2003: Oceanic forcing of Sahel rainfall on interannual to interdecadal time scales. *Science*, **302**, 1027–1030.

Giorgi, F., and P. Lionello, 2008: Climate change projections for the Mediterranean region. *Global Planet Change*, **63**, 90–104.

Haensler, A., S. Hagemann, and D. Jacob, 2011: The role of the simulation setup in a long-term high-resolution climate change projection for the southern African region. *Theor. Appl. Climatol.*, **106**, 153–169.

He, Y. L., J. P. Huang, and M. X. Ji, 2014: Impact of land-sea thermal contrast on interdecadal variation in circulation and blocking. *Climate Dyn.*, doi: 10.1007/s00382-014-2103-y.

Held, I. M., and B. J. Soden, 2006: Robust responses of the hydrological cycle to global warming. *J. Climate*, **19**, 5686–5699.

Hobbins, M., A. Wood, D. Streubel, and K. Werner, 2012: What drives the variability of evaporative demand across the conterminous United States? *J. Hydrometeorol.*, **13**, 1195–1214.

Huang, D.-Q., J. Zhu, Y.-C. Zhang, and A.-N. Huang, 2013: Uncertainties on the simulated summer precipitation over Eastern China from the CMIP5 models. *J. Geophys. Res. (Atmos.)*, **118**, 9035–9047.

Huang, J. P., X. Guan, and F. Ji, 2012: Enhanced cold-season warming in semi-arid regions. *Atmospheric Chemistry and Physics*, **12**, 5391–5398.

Huang, J., P. Minnis, H. Yan, Y. Yi, B. Chen, L. Zhang, and J. K. Ayers, 2010: Dust aerosol effect on semi-arid climate over Northwest China detected from A-Train satellite measurements. *Atmospheric Chemistry and Physics*, **10**, 6863–6872.

Huang, J. P., and Coauthors, 2008: An overview of the semi-arid climate and environment research observatory over the Loess Plateau. *Adv. Atmos. Sci.*, **25**, 906–921, doi: 10.1007/s00376-008-0906-7.

Hughes, L., 2011: Climate change and Australia: Key vulnerable regions. *Regional Environmental Change*, **11**, 189–195.

Hughes, M. K., and H. F. Diaz, 2008: Climate variability and change in the drylands of Western North America. *Global and Planetary Change*, **64**, 111–118.

IPCC, 2013: Climate change 2013: The physical science basis. Stocker, and Coauthors, Eds., *Contribution of Working Group I to the Fifth Assessment Report of the Intergovernmental Panel on Climate Change*, Cambridge University Press, Cambridge, United Kingdom and New York, NY, USA.

Ji, F., Z. H. Wu, J. P. Huang, and E. P. Chassignet, 2014: Evolution of land surface air temperature trend. *Nature Climate Change*, doi: 10.1038/nclimate2223.

Kimoto, M., 2005: Simulated change of the east Asian circulation under global warming scenario. *Geophys. Res. Lett.*, **32**, L16701, doi: 10.1029/2005GL023383.

Kottek, M., J. Grieser, C. Beck, B. Rudolf, F. Rubel, 2006: World map of the Köppen-Geiger climate classification updated. *Meteorol. Z.*, **15**(3), 259–263.

Kumar, D., E. Kodra, and A. R. Ganguly, 2014: Regional and seasonal intercomparison of CMIP3 and CMIP5 climate model ensembles for temperature and precipitation. *Climate Dyn.*, **43**, 2491–2518.

Kusunoki, S., J. Yoshimura, H. Yoshimura, A. Noda, K. Oouchi, and R. Mizuta, 2006: Change of Baiu rain band in global warming projection by an atmospheric general circulation model with a 20-km grid size. *J. Meteor. Soc. Japan*, **84**, 581–611.

Legates, D. R. and C. J. Willmott, 1990: Mean seasonal and spatial variability in gauge-corrected, global precipitation. *International Journal of Climatology*, **10**, 111–127.

Li, S. X., Z. H. Wang, T. T. Hu, Y. J. Gao, and B. A. Stewart, 2009: Nitrogen in dryland soils of China and its management. *Advances in Agronomy*, **101**, 123–181.

Ma, Z. G., and C. B. Fu, 2003: Interannual characteristics of the surface hydrological variables over the arid and semi-arid areas of northern China. *Global Planetary Change*, **37**, 189–200.

Maestre, F. T., R. Salguero-Gómez, and J. L. Quero, 2012: It is getting hotter in here: determining and projecting the impacts of global environmental change on drylands. *Philosophical Transactions of the Royal Society B: Biological Sciences*, **367**, 3062–3075.

Mariotti, A., N. Zeng, J.-H. Yoon, V. Artale, A. Navarra, P. Alpert, and L. Z. X. Li, 2008: Mediterranean water cycle changes: Transition to drier 21st century conditions in observations and CMIP3 simulations. *Environmental Research Letters*, **3**, 044001, doi: 10.1088/1748-9326/3/4/044001.

Meigs, P., 1953: The distribution of arid and semi-arid homoclimates. *UNESCO, Arid Zone Research*, Series 1, Reviews of Research on Arid Zone Hydrology, 203–210.

Middleton, N., and D. Thomas, 1997: *World Atlas of Desertification*. 2nd ed., Arnold, Copublished in the US, Central and South America by John Wiley.

Mitchell, T. D., and P. D. Jones, 2005: An improved method of constructing a database of monthly climate observations and associated high-resolution grids. *International Journal of Climatology*, **25**, 693–712.

Neelin, J., C. Chou, and H. Su, 2003: Tropical drought regions in global warming and El Niño teleconnections. *Geophys. Res. Lett.*, **30**, 2275, doi: 10.1029/2003GL018625.

Nicholson, S. E., Ed., 2011: *Dryland Climatology*. Cambridge University Press, 516 pp.

Penman, H. L., 1948: Natural evaporation from open water, bare soil and grass. *Proceedings of the Royal Society of London. Series A. Mathematical and Physical Sciences*, **193**, 120–145.

Pierce, D. W., T. P. Barnett, B. D. Santer, and P. J. Gleckler, 2009: Selecting global climate models for regional climate change studies, *P. Natl. Acad. Sci. USA*, **106**, 8441–8446.

Reynolds, J. F., and Coauthors, 2007: Global desertification: Building a science for dryland development. *Science*, **316**, 847–851.

Rodell, M., and Coauthors, 2004: The global land data assimilation system. *Bull. Amer. Meteor. Soc.*, **85**, 381–394.

Safriel, U., and Coauthors, 2005: Dryland systems. R. Hassan, R. Scholes, and N. Ash, Eds., *Ecosystems and Human Well-being, Current State and Trends*, Island Press, 623–662.

Schneider, U., A. Becker, P. Finger, 2013: GPCC's new landsurface precipitation climatology based on quality-controlled *in situ* data and its role in quantifying the global water cycle. *Theor. Appl. Climatol.*, **115**, 15–40, doi: 10.1007/s00704-013-0860-x.

Seager, R., N. Naik, and G. A. Vecchi, 2010: Thermodynamic and dynamic mechanisms for large-scale changes in the hydrological cycle in response to global warming. *J. Climate*, **23**, 4651–4668.

Seager, R., and Coauthors, 2007: Model projections of an imminent transition to a more arid climate in southwestern North America. *Science*, **316**, 1181–1184.

Shaw, S. B., and S. J. Riha, 2011: Assessing temperature-based PET equations under a changing climate in temperate, deciduous forests. *Hydrol Process*, **25**, 1466–1478.

Taylor, K. E., R. J. Stouffer, and G. A. Meehl, 2012: An overview of CMIP5 and the experiment design. *Bull. Amer. Meteor. Soc.*, **93**, 485–498.

Thornthwaite, C. W., 1948: An approach toward a rational classification of climate. *Geographical Review*, **38**(1), 55–94.

Trenberth, K. E., A. G. Dai, R. M. Rasmusson, and D. B. Parsons, 2003: The changing character of precipitation. *Bull. Amer. Meteor. Soc.*, **84**, 1205–1217.

Wallace, J. M., Q. Fu, B. V. Smoliak, P. Lin, and C. M. Johnson, 2012: Simulated versus observed patterns of warming over the extratropical Northern Hemisphere continents during the cold season. *Proceedings of the National Academy of Sciences of the United States of America*, **109**, 14337–14342.

Wang, X., J. P. Huang, M. X. Ji, and K. Higuchi, 2008: Variability of East Asia dust events and their long-term trend. *Atmos. Environ.*, **42**, 3156–3165.

Wang, X., J. P. Huang, R. D. Zhang, B. Chen, and J. R. Bi, 2010: Surface measurements of aerosol properties over northwest China during ARM China 2008 deployment. *J. Geophys. Res.*, **115**, D00K27, doi: 10.1029/2009JD013467.

Wang X., W. Pu, J. S. Shi, J. R. Bi, 2015: A comparison of the physical and optical properties of anthropogenic air pollutants and mineral dust over northwest China. *J. Meteor. Res.*, **29**, 180–200, doi: 10.1007/s13351-015-4092-0.

Zeng, N., and J. Yoon, 2009: Expansion of the world's deserts due to vegetation-albedo feedback under global warming. *Geophys. Res. Lett.*, **36**, L17401, doi: 10.1029/2009GL039699.

Zhao, T. B., L. Chen, and Z. G. Ma, 2014: Simulation of historical and projected climate change in arid and semiarid areas by CMIP5 models. *Chinese Science Bulletin*, **59**, 412–429.